Chapter 1

Introduction

1.1 Compact extragalactic radio sources

Fourteen years after the pioneer work by K.G. Jansky (Jansky 1932), observations of rapid amplitude variations at low frequencies lead to the discovery of the *discrete radio sources* (Hey, Parsons, and Phillips 1946). Thought to be due to the intrinsic intensity fluctuations, these variations were initially ascribed to radio emission from stars in our galaxy, because of the extremely short timescales ($\sim$1 min) of the observed variability. After three of the strongest radio sources were identified with nearby galaxies (Bolton and Stanley 1949; Smith 1951; Baade and Minkowski 1954), the extragalactic nature of the discrete sources was recognized. Incoherent synchrotron emission produced by a nonthermal population of relativistic electrons was suggested to explain the discrete sources (Alfvén and Herlofsen 1950; Schklovsky 1953).

The subsequent discovery of *quasars* (Schmidt 1963) — extremely luminous extragalactic objects associated with ultra compact, variable radio sources (Dent 1965) suggested that the observed phenomena could be related to the immediate vicinity of the core of a host galaxy. The phenomenon of activity occurring in a significant fraction of galactic nuclei (called *active galactic nuclei*, AGN) has been studied extensively over the last decades. However, it was not until the development of the *aperture synthesis* method (Ryle & Hewish 1960), the introduction of *Very Long Baseline Interferometry* (VLBI) (cf. Matveenko, Kardashev, and Sholomitskii 1965; Clark *et al.* 1968a,b), and application of the *phase closure* method (Jennison 1958) to VLBI (Rogers *et al.* 1974) that mapping with milliarcsecond resolution became possible, and parsec–scale structures were directly observed in extragalactic objects.

In 1971, VLBI observations lead to the discovery of *superluminal expansion* in compact extragalactic radio sources (Moffet *et al.* 1971; Cohen *et al.* 1971; Whitney *et al.* 1971). Since 1978, VLBI observations have been providing a substantial inflow of information on morphology, kinematics, physical conditions, and long–term evolutions in the parsec–scale regions around galactic nuclei (see Zensus and Pearson 1987). Complemented by data from other types of radio observations (single dish, linked interferometers) and observations made in other parts of the electromagnetic spectrum, VLBI observations have yielded a detailed picture of AGN, and allowed for the development of elaborate physical models of the phenomenon.

The most successful theoretical models among those suggested to explain the observed manifestations of AGN are based on three fundamental assumptions: relativistic beaming (Shklovsky 1963), relativistic injection from galactic nuclei (Rees 1966), and accretion of matter onto a central black hole (see Begelman, Blandford, and Rees 1984). The initial assumption of spherically symmetrical expansion (e.g.van der Laan 1963; Rees 1967; Burbidge 1967) has been superseded by the axially symmetrical jet geometry (Rees 1971; Longair, Ryle, and Scheuer 1973; Blandford and Rees 1974). The latter gives rise to the *relativistic shock* model (Blandford & Königl 1979) and to the two–fluid model (Sol *et al.* 1989).

Relativistic shocks in a fluid jet with an ultra relativistic equation of state (Hughes, Aller, and Aller 1985) were used to explain the integrated flux and polarization variations in BL Lac, 3C 279, OT 081 (Hughes *et al.* 1990), and OJ 287 (Cawthorne & Wardle 1988). A modification of the relativistic shock model, the *shock–in–jet* model (Marscher & Gear 1985) was applied to the total radio emission of 3C 273 (Marscher *et al.* 1991). Relativistic shocks in helical jets were modeled (Gómez *et al.* 1994) and applied to 3C 84 and 3C 345 (Steffen *et al.* 1995). More recently, another modification of the relativistic shock model (Kolgaard *et al.* 1990; Cawthorne *et al.* 1993) was used to interpret the kinematic and polarization properties of the parsec–scale jet in 3C 345 (Wardle *et al.* 1994).

The two–fluid model was used to describe the formation (Henri & Pelletier 1991), stability, and confinement (Pelletier & Sol 1992) of a relativistic electron–positron beam. The model is able to account for the observed helical geometry and long–term flux evolution of the parsec–scale jets (Lobanov & Zensus 1994). For 3C 273, short–term optical variability and related changes of the jet kinematics were described by the precessed electron–positron beam, in the framework of the two–fluid model (Roland, Teyssier, and Roos 1994).

1.2 Parsec–scale regions of AGN

Despite an extended account of observational and theoretical studies, there are still several unresolved issues about physics of parsec–scale structures in AGN:

Evolutions of the jet constituents have been studied in detail, for a few of the most prominent sources such as 3C 345 (Biretta, Moore, and Cohen 1986; Zensus, Cohen, and Unwin 1994), 3C 273 (Krichbaum 1990), BL Lac (e.g.Mutel and Phillips 1987) and others (see Zensus and Pearson 1987, 1990). The time periods covered by the most of the studies do not exceed five years. The studies have been limited largely to deriving the kinematic properties of the *enhanced emission regions* (or *bright components*) embedded in the jet. More detailed knowledge of the jet evolution including studies of long–term kinematic evolution, flux evolution and spectral evolution is crucial for understanding the physical processes occuring in the parsec–scale regions of

AGN.

No extensive studies have been done concerning synchrotron spectra of the jets and their evolution. Specifics of VLBI makes obtaining reliable spectral information a non–trivial task. The *scaled array* technique used in linked interferometers for more than two decades cannot be implemented in VLBI observations. Calibration errors and poor and uneven *uv*–coverages at different frequencies can contaminate results of a spectral analysis. Because of these factors, information about synchrotron spectra of the jets is mostly limited to spectral indices derived for bright components of the jet.

The majority of physical models describing the evolution of the jet have so far been applied to the total emission from the source (e.g. Marscher, Gear, and Travis 1991). In some cases, analysis of the total emission made it possible to predict the expected source structure on parsec scales (e.g. Hughes, Aller, and Aller 1989b). Shock models experience certain difficulties explaining extended life times of the bright components. These difficulties suggest that there might be some other mechanism providing reacceleration of the jet plasma, after a shock has become weak. Thus there is also the question about the extension of parsec–scale region over which the shock models are applicable.

The role of non–shock mechanisms (Fermi processes (Kirk and Schneider 1987), turbulent acceleration (Conçalves *et al.* 1993), thermal plasma heating and $e^{\pm}$ pair production (Rose *et al.* 1987)) in the reacceleration of relativistic plasma in the jet, and in the extended evolution of the jet emission is not well understood. An extended lifetime of the jet enhanced emission regions in 3C 345 may be an indication of importance of the non–shock emission mechanisms (see Königl 1981).

1.3 3C345

The thesis work represents an in depth study of parsec–scale regions observed in the radiosource 3C345. The quasar 3C345 (z=0.595, Hewitt and Burbidge 1993) is one of the best examples of a variable AGN exhibiting high activity in all wavebands and remarkable structural and flux variability on the parsec scales around the very compact unresolved radio core. The continuum spectrum is flat up to 10 GHz, and steepens towards higher frequencies as $\nu^{(-0.9)-(-1.4)}$ (Bregman *et al.* 1986). The long–term optical variability of the source is possibly quasi–periodical over ≈1560 days (Babadzhanyants and Belokon' 1984; Kidger 1990), although there is an argument that the light curve is the result of a non–linear and non–stationary stochastic process (Vio *et al.* 1991). The time–scale of variability becoming progressively shorter with higher frequencies may lead to a suggestion of at least two emitting regions in the source core (Bregman *et al.* 1986).

The radio emission of 3C345 has been closely monitored over the last decade using VLBI (cf. Unwin *et al.* 1983; Biretta, Moore and Cohen 1986, hereafter BMC86; Unwin and Wehrle 1992; Matveenko *et al.* 1992; Zensus, Cohen and Unwin 1994, hereafter ZCU95) and single dish observations (cf. Aller *et al.* 1985; Hughes *et al.* 1991a; Teräsranta *et al.* 1991). The VLBI monitoring has been performed primarily at 5, 10.7, and 22.3 GHz, with several observations made at 1.4, 2.3, 8.4, 43, and 89 GHz. The single dish monitoring programs include frequent flux measurements at 5, 8, and 15 GHz at the University of Michigan Radio Astronomy Observatory (UMRAO), and at 22 and 37 GHz at the Metsähovi Radio Research Station, Finland. Also, the source has been monitored at 2.7 and 8.1 GHz with the Green Bank Interferometer since 1979 (Waltman *et al.* 1991).

The major results of these programs have appeared in studies of the long-time variability (Hughes *et al.* 1992), and kinematics of the VLBI scale jets (ZCU95). The relativistic jet model introduced by Blandford and Rees (1978), and later developed in a number of works (cf. Hughes, Aller, and Aller 1991; Marscher 1987; Valtaoja *et al.* 1992) was applied to the VLBI observation of 3C345, to explain the enhanced emission regions in the jet. ZCU95 derive physical conditions of the jet from a scenario combining the inhomogeneous–jet model of Königl for the core with homogeneous spheres for the superluminal components. Steffen *et al.* (1995) apply a helical jet model to explain the observed component trajectories and flux variations. Rabaça and Zensus (1994) show that flux evolution of the jet component C4 is consistent with a strong shock concentrated in a narrow region. In recent papers by Brown *et al.* (1994) and by Wardle *et al.* (1994), the relativistic shock model is applied to the kinematic and polarization evolution of the jet.

1.4 Structure of the dissertation

This dissertation is the continuation of a VLBI monitoring program for 3C 345 started in 1979. Previous observations have covered the time period from 1979 to 1988 (Biretta, Moore, and Cohen 1986; Zensus Cohen and Unwin 1995). This work adds 13 new VLBI observations of 3C 345 made at 1.3, 2.8, 3.6, and 6cm, extending the analysis of the jet evolution until the end 1993. Overall, 14 years of regular observations of the source — the longest known time period of VLBI monitoring — have been analyzed. The observations and post–processing procedures are summarized in Chapter 2. An overview of the previous observations is also presented.

In Chapter 3, the jet kinematics are described. The trajectories of the jet components and a method of their calculations are presented. Two simple jet models — the curved jet with constant velocity and the straight jet with acceleration — are discussed.

Chapter 4 deals with the jet synchrotron spectrum. We discuss spectral index mapping and develop a method that can be implemented for spectral index mapping using quasi–simultaneous multifrequency VLBA observations.

We present several spectral index maps obtained from the latest observations. We consider the effect of a frequency dependent shift of the core position and its influence on the spectral index maps. We measure the shift for 3C 345 and apply the necessary corrections to the spectral index maps.

A Monte Carlo simulation based method of discrete and continuous broadband synchrotron spectrum fitting has been developed and implemented. Using this method, the basic spectral parameters (the turnover frequency, peak flux density and integrated flux) have been calculated for the jet components. The distribution of the turnover frequency along the jet has been mapped for the first time. In the turnover frequency distribution maps, evidence for a relativistic channel and a strong shock front are found.

In Chapter 5, we describe the long–term evolution of the jet. The kinematic, flux, luminosity, and spectral aspects of evolution are considered. We present correlations discovered between kinematic and spectral parameters of the jet. The luminosity evolution along the jet is studied for different kinematic scenarios.

Chapter 6 presents a comparison of the observed evolutions and correlations with predictions by the shock–in–jet model. With the help of the data from single dish monitoring (Teräsranta and Valtaoja 1994, personal communications), we estimate the extent of a region where the shock models can be applicable. We develop a modification of the shock–in–jet model to account for a variable Doppler factor along the jet. The kinematic and spectral changes observed in the most prominent jet components are compared with the model predictions. Conclusions on the possible physical nature of these components are made. Presence of the forward and reverse shock in the jet is suggested.

Chapter 7 gives a summary of the observational and theoretical results of the thesis work.

Chapter 8 contains an appendix with the model fits from the older VLBI observations of 3C345.

1.5 Main results

The basic results achieved through the thesis work can be summarized as follows:

1. A detailed physical picture of the parsec–scale regions in 3C 345 is presented. A combined study of the jet kinematics and radio spectrum has been performed. Observational manifestations of the enhanced emission regions embedded in the jet were studied and compared with theoretical predictions. Various technical and methodological aspects of determining the spectral characteristics of parsec–scale regions in AGN are discussed.

2. 13 new VLBI observations constituting a five year extension of the VLBI monitoring of 3C 345 have been made. The High dynamic range of the maps enabled studies of the jet morphology and evolution. Added to the previous VLBI observations of 3C 345, the overall data constitute the longest VLBI monitoring period of a single source.

3. From the overall data, the long–term evolution of the jet has been reconstructed for a period of time from 1979 to 1993. The kinematic, flux, and spectral changes have

been studied. Relations between jet kinematics and emission have been observed.

4. Spectral index mapping with VLBI is discussed. A method of spectral index mapping using quasi–simultaneous multifreqeuncy VLBA observations is proposed. Several spectral index maps of 3C345 have been produced, from the VLBI data. The effect of a frequency dependent shift of an optically thick core is discussed and measured. Based on the measurements, corrections to spectral index maps are applied.

The mapping method and corrections for the frequency dependent shift can be used for spectral index mapping of various core–jet type compact sources.

5. A method of broadband synchrotron spectrum fitting has been developed and implemented for discrete and continuous fitting of VLBI data. The method of continuous spectral fitting can be used for restoring spectral parameters of compact jets in other sources.

6. Spectral parameters (turnover frequency, peak flux density, integrated flux) and luminositites of the jet bright components are derived, on the basis of the fit. Their evolutions are studied. Relationships between the spectral, flux and kinematic evolutions are investigated. 4 VLBA observations have been made quasi-simultaneously at 5, 8.4, 15.4 and 22.3 GHz, and the data have been used for obtaining the first map of the turnover frequency distribution. The obtained turnover frequency distribution map shows possible locations of the relativistic channel and Kelvin-Helmholtz instability driven patterns in the extended jet. The magnetic field distribution is measured in the core, using the turnover frequency and turnover flux maps. A region with highly compressed magnetic field is shown to be coincident with the location of a strong shock near the core fo the jet.

7. Modifications of the shock–in–jet model are made so as for the model to account for changes of Doppler boosting along the jet. Considered are the effects of variable Doppler boosting on the spectral evolution of the jet.

8. The predictions by the shock–in–jet model are compared with the observed flux, kinematic, and spectral evolutions. Ranges of applicability of the shock based emission schemes are estimated. Physical parameters in the jet enhanced emission regions are estimated, allowing for a suggestion of the presence of the forward and reverse shocks in the jet.

9. On the basis of the combined study of the jet physics, we suggest there may exist a transition zone in the jet characterized by the transition from the shock–dominated to the plasma interaction–dominated emission regime.

Chapter 2

VLBI Observations

2.1 Introduction

The observations incorporated in this dissertation are a part of the ongoing VLBI monitoring program of the quasar 3C345. The observations cover the time period from March 1989 to November 1993. 13 VLBI observations of 3C345 were performed with the Global VLBI network, using the Mark II (Clark 1973) and Mark III (Rogers *et al.* 1983) recording systems. All Mark II observations were correlated at the Block-2 correlator (operated jointly by California Institute of Technology and Jet Propulsion Laboratory). Correlations of the Mark III observations were done at the VLBA[1] correlator (Array Operation Center, Socorro, New Mexico). Post–correlation processing of the data included fringe fitting, amplitude calibration, and imaging. Fringe fitting and amplitude calibration were done using Astronomical Image Processing System [AIPS] a software developed at the National Radio Astronomy Observatory [NRAO]. The imaging was done with assistance of AIPS, Caltech VLBI software (Pearson 1991), and the differential mapping software DIFMAP (Shepherd *et al.* 1994)

For the purpose of consistency of the data, 15 older datasets from the observation epochs between 1984 and 1988 (Zensus *et al.* 1995a) were also remapped using DIFMAP.

The earlier data covering the epochs from 1979 to 1984 were taken from Biretta, Moore and Cohen (1986)

In this chapter we present a brief review of the technique of VLBI, and describe the post–correlation processing of the data.

2.2 Antenna performance and data acquisition

Theoretical reviews of underlying concepts of optics and interferometry can be found in Born and Wolf (1980) and Thompson, Moran, and Swenson (1991). Elaborate presentations of the modern state of radio interferometry and synthesis imaging are

[1]VLBA – Very Long Baseline Array, operated by the National Radio Astronomy Observatory

given in Perley, Schwab, and Bridle (eds.) (1991) and Zensus, Diamond, and Napier (eds.) (1995b). We use these sources, to compile a brief introduction into the topics of antenna performance and data acquisition relevant to further discussion of the VLBI observations.

2.2.1 Spatial coherence function

For a radio source producing a variable electric field $\mathbf{E}(\mathbf{R}, t)$ (Figure 2.1), the field at the source location can be represented as a sum of *quasi–monochromatic components* $\mathbf{E}_\nu(\mathbf{R})$ which are the coefficients of the Fourier expansion of the electric field. The corresponding electric field at the observer's location $\mathbf{r}$is:

$$\mathbf{E}_\nu(\mathbf{r}) = \int P_\nu(\mathbf{R}, \mathbf{r})\mathbf{E}_\nu(\mathbf{R})dS. \tag{2.1}$$

The integral indicates a superposition of the field components from every point of the source. Integration must be done over the whole source. The function $P_\nu(\mathbf{R}, \mathbf{r})$ describes propagation of the electric field from $\mathbf{R}$ to $\mathbf{r}$. In vacuum

$$P_\nu = \frac{1}{|\mathbf{R} - \mathbf{r}|}\exp(2\pi i\nu|\mathbf{R} - \mathbf{r}|/c), \tag{2.2}$$

so that a quasi–monochromatic component of the field can be written as:

$$\mathbf{E}_\nu(\mathbf{r}) = \int \frac{\mathbf{E}_\nu(\mathbf{R})e^{2\pi i\nu|\mathbf{R}-\mathbf{r}|/c}}{|\mathbf{R} - \mathbf{r}|}dS. \tag{2.3}$$

The field at two different receiving locations $\mathbf{r}_1$ and $\mathbf{r}_2$ is correlated, and this correlation is given by the expectation of the product of the fields at the given locations:

$$\mathbf{V}_\nu(\mathbf{r}_1, \mathbf{r}_2) =< \mathbf{E}_\nu(\mathbf{r}_1)\mathbf{E}^*_\nu(\mathbf{r}_2) >, \tag{2.4}$$

where the asterisk indicates the complex conjugate.

In most of cases it is plausible to assume that the *emitted* fields are spatially incoherent (that is, $< \mathbf{E}_\nu(\mathbf{R}_1)\mathbf{E}_\nu(\mathbf{R}_2) >\equiv 0$ for $\mathbf{R}_1 \neq \mathbf{R}_2$). In further considerations, terms of order $|\mathbf{r}/\mathbf{R}|$ can be safely ignored. Using a unit vector, $\mathbf{s} = \mathbf{R}/|\mathbf{R}|$, in the direction of $\mathbf{R}$, and substituting the areal element of integration, dS, with the element of solid angle, $d\Omega$, we can rewrite (2.4) as:

$$V_\nu(\mathbf{r}_1, \mathbf{r}_2) = \int I_\nu(\mathbf{s})e^{-2\pi i\nu\mathbf{s}\cdot(\mathbf{r}_1-\mathbf{r}_2)}d\Omega\,, \tag{2.5}$$

where $I_\nu = |\mathbf{R}|^2 < |\mathbf{E}| >^2$ – the observed *intensity* of the radiation field. This function, V_ν, is the *spatial coherence function* of the field $\mathbf{E}_\nu(\mathbf{r})$, and it can be directly measured by interferometric devices.

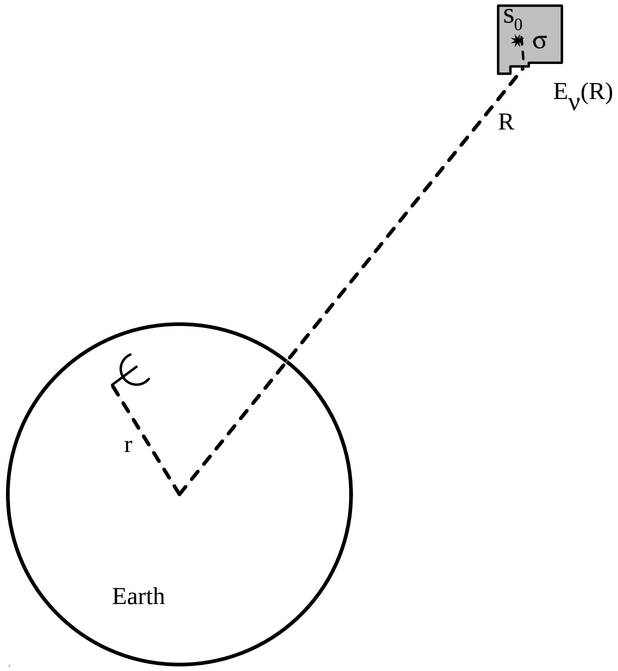

Figure 2.1: Basic picture of radio source – antenna geometry.

In the case of the angular size of radiating object being small, we can use an expansion of the unit vector $\mathbf{s} = \mathbf{s}_0 + \sigma$ (see Figure 2.1). Introducing the coordinate system (u, v, w) in which $\mathbf{s}_0 = (0, 0, 1)$, we can rewrite (2.5)

$$V_\nu(u, v) = e^{-2\pi w} \int\int I_\nu(\xi, \eta) e^{-2\pi i[u\xi + v\eta + w(\zeta - 1)]} d\xi d\eta, \tag{2.6}$$

where ξ, η, and ζ refer to the components of the vector $\mathbf{s}$. Since all VLBI measurements are confined to the plane (ξ, η), ζ can be assumed a unity, so that

$$V_\nu(u, v) = \int\int I_\nu(\xi, \eta) e^{-2\pi i(u\xi + v\eta)} d\xi d\eta \tag{2.7}$$

Equation (2.7) describes the basic relation between quantities described in the *spatial frequency domain* (u, v), and those in the *image domain* (ξ, η). Because antenna elements are not ideal, the *primary beam* or *normalized reception pattern*, $G_\nu(\xi, \eta)$ must be included into the integral in (2.7), in order to account for the directional sensitivity of the elements.

2.2.2 Data acquisition

A simplistic overview of an interferometer is given in Figure 2.2. Signals, U_1, U_2 from the two antenna elements are each processed by filters with frequency responses H_1, H_2, and then cross correlated. An antenna with angular reception pattern $G_\nu(\theta)$

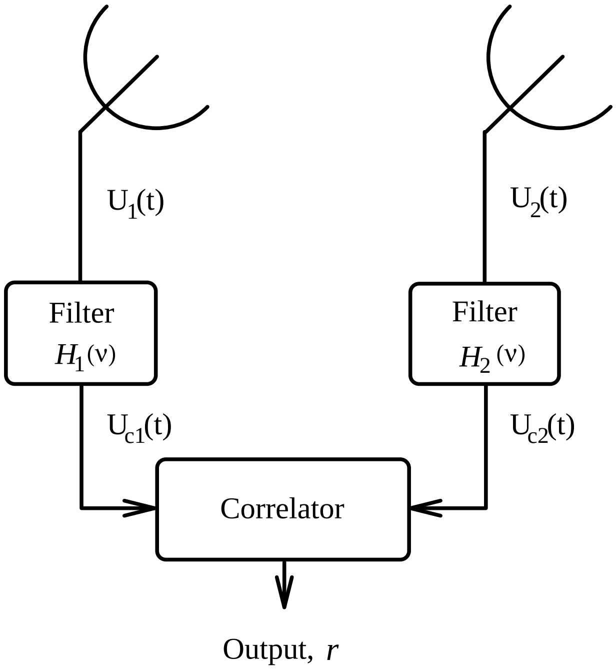

Figure 2.2: Simple interferometer.

responding to a radio source electric field distribution $E_\nu(\theta)$ will produce an output

$$U_\nu = \int E_\nu(\theta) G_\nu(\theta) d\theta \tag{2.8}$$

In the filter, the output of the antenna is mixed with a local oscillator signal and is put through one or more intermediate frequency amplifiers. The outputs of the two filters in the Figure (2.2)

$$U_{c1}(\nu) = U_1(\nu) H_1(\nu), \quad U_{c2}(\nu) = U_2(\nu) H_2(\nu) \tag{2.9}$$

The cross correlation of these two signals in the correlator yields

$$r(\tau) = \lim_{T\to\infty} \frac{1}{2T} \int U_{c1T}(t) U^*_{c2T}(t-\tau) dt \tag{2.10}$$

The subscript T indicates the truncation applied to the time variability of the subscripted functions. The delay τ reflects the source geometry with respect to the two antennas and the various instrumental delays. These delays are calculated and corrected for the expected delays induced by the interferometer, earth rotation, antenna clock rate and the atmosphere. The errors in the calculated delays are corrected using the technique of *fringe fitting*.

2.3 Fringe fitting and amplitude calibration

2.3.1 Fringe fitting

A number of errors can affect the delays obtained from the correlation: errors in the source or antenna position used, errors in the earth model, errors in the clock epoch and rate at each antenna, errors in the atmospheric model. The phase errors $\Delta\phi_{1,\nu}$ caused by errors in the delays are:

$$\Delta\phi_{t,\nu} = 2\pi\nu d\tau_t \tag{2.11}$$

In the time and frequency domain, a first order expansion of the error in interferometer phase is:

$$\Delta\phi_{t,\nu} = \phi_0 + \left(\frac{\partial\phi}{\partial\nu}\Delta\nu + \frac{\partial\phi}{\partial t}\Delta t\right), \tag{2.12}$$

where ϕ_0 is the phase error at the reference time and frequency, $\partial\phi/\partial\nu$ is the *delay residual*, and $\partial\phi/\partial t$ is the *delay rate*. The equation (2.12) holds for each individual antenna. The baseline dependent errors between any two antennas i and j can be written as:

$$\Delta\phi_{i,j} = \phi_{i,0} - \phi_{j,0} + \left(\left[\frac{\partial\phi_i}{\partial\nu} - \frac{\partial\phi_j}{\partial\nu}\right]\Delta\nu + \left[\frac{\partial\phi_i}{\partial t} - \frac{\partial\phi_j}{\partial t}\right]\Delta t\right) \tag{2.13}$$

Various techniques used for estimating the delay rates and delay residual are referred to as *fringe fitting*. For the VLBI data presented in this dissertation, "global" fringe fitting (Schwab and Cotton 1983, Walker 1989a,b) was used. Global fringe fitting applies equation (2.13) to all data, and estimates the antenna-based phase, delay rate, and delay residuals. The details of the used procedure can be found in Cotton (1995).

2.3.2 Amplitude calibration

The measured visibility V_{ij} between antennas i and j can be expressed as:

$$V_{ij}(\nu,t) = \mathcal{G}_i(\nu,t)\mathcal{G}_i^*(\nu,t)V'_{ij}(\nu,t) + \epsilon_{ij}, \tag{2.14}$$

where V'_{ij} is the true visibility of the source on the $i-j$ baseline, ϵ_{ij} is the thermal noise on the baseline, and $\mathcal{G}_i$, $\mathcal{G}_j$ are the complex antenna gains ($\mathcal{G}(\nu,t) = a(\nu,t)e^{i\phi(\nu,t)}$). For the amplitude calibration, the phase terms of the antenna gains can be omitted. The thermal noise term can be ignored. Then, to calibrate the observed visibility, we can use equation (2.14), and obtain

$$S_{ij}(\nu,t) = \frac{A_{ij}(\nu,t)}{a_j(\nu,t)a_j(\nu,t)} \tag{2.15}$$

Here we have equated the amplitude of the true visibility V'_{ij} with the calibrated, correlated flux density S_{ij}. A_{ij} represents the measured visibility amplitude, and is usually the raw correlation coefficient from the correlator. Equation (2.15) can be rewritten in more practical terms as:

$$S_{ij} = A_{ij} b \sqrt{\frac{T_{s_i} T_{s_j}}{K_i K_j}}, \tag{2.16}$$

where b is the correlator dependent factor that accounts for digitization losses, K_i, K_j are the antenna sensitivities measured in K/Jy, and T_i, T_j are the antenna system temperatures in Kelvins. The antenna sensitivities are measured systematically; the system temperatures are logged for every experiment. The b-factors are determined for each correlator individually. We have used $b = 13.53$ for the Caltech Block-2 correlator. For the VLBA correlator $b = 1$.

If the observed source is strong, the antenna temperatures T_a can be measured and used for the amplitude calibration, in place of the antenna sensitivities. The calibration formula in this case is:

$$S_{ij} = A_{ij} b S_{tot} \sqrt{T_{s_i} T_{a_i}} \sqrt{T_{s_j} T_{a_j}}, \tag{2.17}$$

where S_{tot} is the source total flux density.

More extensive discussions of the calibration procedures can be found in Walker (1989a) and Moran and Dhawan (1995).

2.4 Imaging

2.4.1 Deconvolution

If interferometer phases and delays have been calculated, and visibilities have been calibrated, then we can use the relation (2.7) for finding the true intensity distribution

$$I_\nu(\xi, \eta) = \int \int V_\nu(\xi, \eta) e^{2\pi(u\xi + v\eta)} du dv \tag{2.18}$$

Since the spatial coherence function V_ν is not known everywhere, a sampling function $S(u, v)$ (also called the *uv-coverage*) has to be introduced into equation (2.18)

$$I^D_\nu(\xi, \eta) = \int \int V_\nu(u, v) S(u, v) e^{2\pi(u\xi + v\eta)} du dv \tag{2.19}$$

I^D_ν is the *dirty image* related to the true intensity distribution I_ν by the Fourier convolution theorem:

$$I^D(\xi, \eta) = B(\xi, \eta) * [I(\xi, \eta) + N(\xi, \eta)], \tag{2.20}$$

where $*$ represents deconvolution, $N(\xi,\eta)$ describes the noise in the image, and B (called the *point spread function* or *synthesized beam*) is the two–dimensional Fourier transform of the sampling function $S(u,v)$

$$B(\xi,\eta) = \int\int S(u,v) e^{2\pi i(u\xi+v\eta)} du dv \tag{2.21}$$

Because the VLBI sampling functions are finite and poorly defined, non–linear deconvolution methods and self–calibration techniques are used in to refine the *primary solution* I^D. The two deconvolution methods widely used in radio interferometry are the *Maximum Entropy Method* (MEM) and the "CLEAN" algorithm. Reviews of the MEM technique can be found in Narayan and Nityananda (1986) and Cornwell and Braun (1989).

The "CLEAN" algorithm was introduced by Högbom (1974), and modified later by Clark (1980) and Schwab and Cotton (1983). The DIFMAP implementation of "CLEAN" (Shepherd *et al.* 1994) was used for producing all images presented in the dissertation. The "CLEAN" method and its modifications provide a solution to the convolution equation (2.20) by representing the true intensity distribution by a number of point sources (δ–*functions*). The field of view outside the area selected for the source search is assumed to be empty. The final deconvolved image is the sum of the the point components convolved with an artificial "CLEAN" beam. Detailed discussions of the "CLEAN" algorithm can be found in Wilkinson (1989), Cornwell and Braun (1989), and Cornwell (1995).

Figure 2.3 gives an example of sampling function, point spread function, dirty image, and clean image. All pictures are produced from the VLBI data for 3C345 observed on June 15 1992 at 5 GHz.

2.4.2 Closure quantities

In VLBI experiments, it is impossible to achieve an external calibration of the interferometer amplitudes and phases. Because of this, imaging with the VLBI relies largely on the concepts of *closure quantities.*

If we substitute complex gains in (2.14) with their explicit expressions, we can write for the visibility observed on the $i-j$ baseline

$$V_{ij} = a_i a_j e^{i(\phi_i - \phi_j)} V'_{ij} + \epsilon_{ij} \tag{2.22}$$

Time and frequency dependences of all terms are regarded as implicit.

Ignoring the noise terms ϵ_{ij}, we can relate the phases of any three antennas, and amplitudes of any four antennas so that the antenna dependent terms in the measured amplitudes and phases will be cancelled (Jennison 1958, Twiss *et al.* 1960, Readhead *et al.* 1980) We assume that the relation

$$V'_{ij} = A_{ij} e^{i\psi_{ij}} \tag{2.23}$$

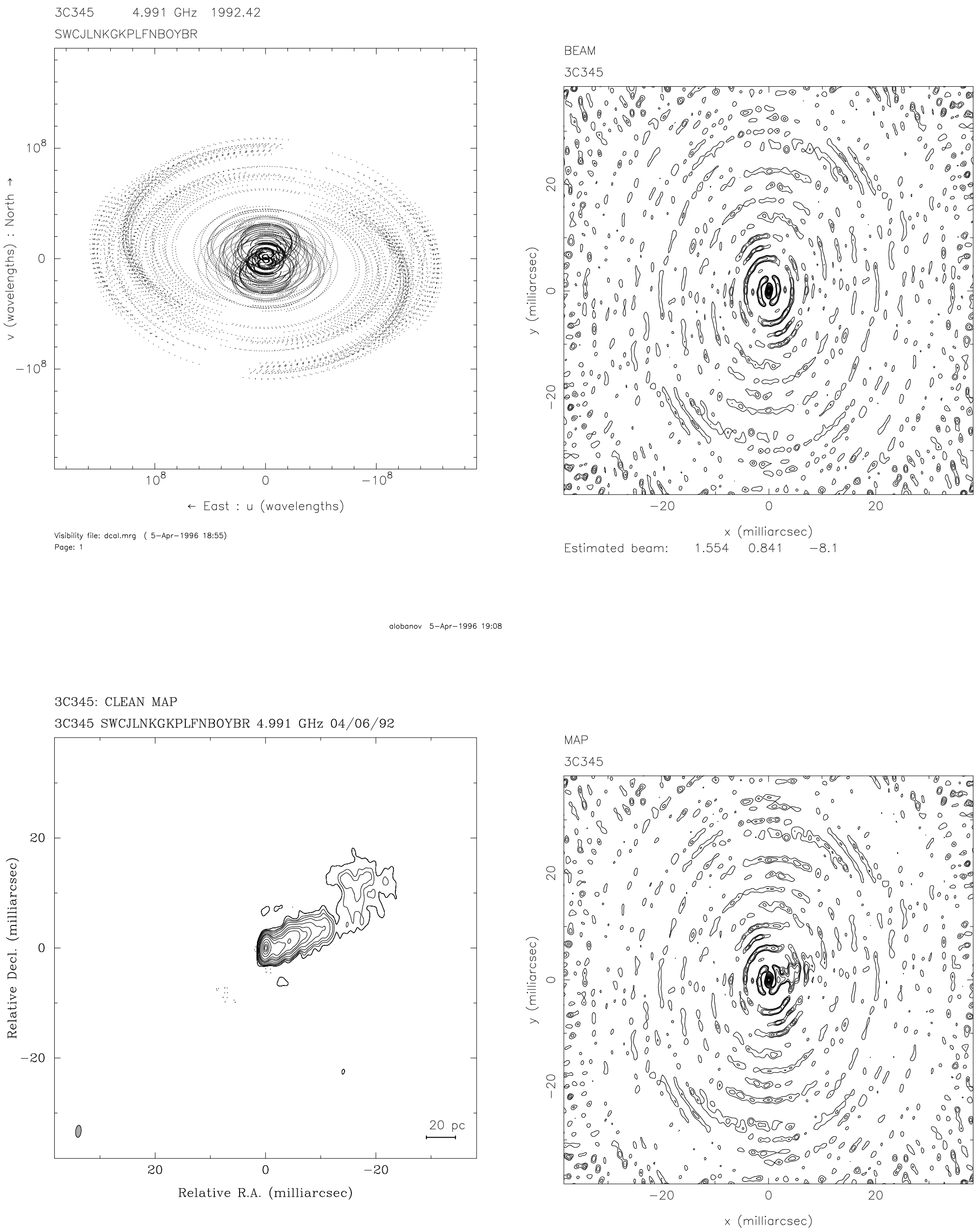

Figure 2.3: Clockwise from the upper left panel: the *uv*–coverage (sampling function), the synthesized beam, the dirty map, and the "CLEAN" map for the observation of 3C345 made on June 15 1992 at 5 GHz with the Global VLBI array. Contours in all three images are corresponding to -0.1, 0.1,0.2,0.3,0.5,1,2,3,5,10,25,50,75, and 90% of the peak level of the corresponding image.

represents the ideal complex correlation coefficient corresponding to one spatial frequency. Then, from (2.22), the *closure phase* of the antenna set $(1, 2, 3)$ is given by

$$C_{123} = \phi_{12} + \phi_{23} - \phi_{13} = \psi_{12} + \psi_{23} - \psi_{13} = C'_{123} \tag{2.24}$$

In the sum represented by (2.24) all antenna–based phase errors cancel. The closure phase is the argument of the *bispectrum*

$$\mathcal{B} = V(u,v)V(u',u')V(-u - u', -v - v') \tag{2.25}$$

of the sky brightness distribution. From (2.25), it follows that the closure phase is a function of four variables, namely two positions in the uv–plane. Due to the poor sampling of the uv–plane the information preserved by the closure phase relation can be ambiguous. The ambiguity can be overcome with increasing the number of antennas, since the fraction of the visibility information available from the closure phase is $(N-2)/N$, where N is the number of antennas (Pearson 1995).

Another observable closure quantity is the *closure amplitude* Γ_{1234}. It can be defined for any four antennas so that the antenna gains will cancel:

$$\Gamma_{1234} = \frac{|V_{12}|\ |V_{34}|}{|V_{13}|\ |V_{24}|} = \frac{A_{12}A_{34}}{A_{13}A_{24}} \tag{2.26}$$

The closure amplitude, therefore, is a function of six variables (three positions in the uv–plane); and the fraction of information that can be recovered from the closure amplitude is related to the number of antennas as $(N-3)/N-1)$.

Thus, from (2.24)–(2.26), apart from the noise, the observed and the true closure quantities should be identical. This property of the closure quantities makes them useful constraints during the restoration of the true intensity distribution. Both closure phases and closure amplitudes are used during the *self–calibration.*

2.4.3 Self–calibration

Self–calibration is an iterative process of finding a suitable model, $\hat{I}$ such that its Fourier transform

$$\hat{V}_{ij}(u,v) = \int\int \hat{V}_{ij}(\xi,\eta)e^{-2\pi i(u\xi+v\eta)}d\xi d\eta \tag{2.27}$$

reproduces the observed visibilities $V_{ij}(u,v)$ to within the noise level. This is usually achieved by minimization of a certain functional $\mathcal{S}$ containing the model and observed visibilities, and the complex antenna gains. The most common form of this functional is:

$$\mathcal{S} = \sum_k \sum_{i,j;i\neq j} w_{ij}(t_k) \left| V_{ij}(t_k) - \mathcal{G}_i(t_k)\mathcal{G}_j^*(t_k)\hat{V}_{ij}(t_k)\right|^2 \tag{2.28}$$

(Schwab 1980), where w_{ij} are weights reflecting the signal-to-noise ratio of the corresponding visibility. Minimization of $\mathcal{S}$ produces solutions for the antenna gains, and allows for corrections of the phase and amplitude errors incorporated into the observed visibilities. The corrected visibility is:

$$V_{ij,corr}(t) = \frac{V_{ij}(t)}{\mathcal{G}_i(t)\mathcal{G}_j^*(t)} \tag{2.29}$$

The new model can be obtained by deconvolution of the corrected data, and used in the next iteration of self–calibration. Self–calibration has been shown to converge to a unique solution, for most of the VLBI observations with large number of antennas, good a priori calibration, and fairly simple source structure. Advanced discussions on the topic of self–calibration are given in Cornwell and Fomalont (1989), and Cornwell (1995).

Figures 2.4–2.7 illustrate the capabilities of deconvolution and self–calibration. In Figure 2.4, we plot the amplitude calibrated data at 22.3 GHz (3C345; November 11, 1992) before the self–calibration. The top panel shows the raw amplitudes, the raw phases are plotted in the bottom panel. In the next figure (Figure 2.5), the final self–calibrated data set (top) and its "CLEAN" model (bottom) are plotted. Figure 2.6 shows the same comparison for phases. The model follows self–calibrated amplitudes and phases very closely, which is reflected in the resulting low RMS noise level ($\approx$ 3 mJy) and high dynamic range (1770:1) of the map obtained from this data set (the map will be discussed in Section 2.6). Figure 2.7 presents projections of the self–calibrated and model amplitudes onto various position angles in the sky. The double structure of the source is clearly visible in all the plots, and the source extension along the P.A.$\approx$86 can be guessed from the shape of the projection onto this position angle.

2.4.4 Model fitting

Model fitting is a technique which is generally used for solving the inverse problems in which the true distribution of a certain variable needs to be recovered from the measured distribution. In its application to VLBI, model fitting produces a parametric model of sky brightness distribution and calculates the expected measurements. These calculations are compared with the actual measurements, and the discrepancies between measurements and model predictions are used for adjusting the model. The *least squares* implementation of the *maximum likelihood* is used for model fitting VLBI data. That is, the fitting is being achieved by minimizing the following sum:

$$\chi^2 = \sum_{i=1}^{N} \left(\frac{V_(u_i, v_i) - F(u_i, v_i; a_1, ..., a_K)}{\sigma_i} \right)^2 \tag{2.30}$$

where V and F are the observed and predicted distributions, and $a_1, ...a_K$ are the model parameters. The "grid search" (Bevington & Robinnson 1992) and the Levenberg–Marquardt method (see Press *et al.* 1992) are used for minimization of χ^2 with